

Interactions between clear-air reflective layers and rain observed with a boundary layer wind profiler

S. A. Cohn and R. R. Rogers

Department of Atmospheric and Oceanic Sciences, McGill University, Montreal, Quebec, Canada

S. Jascourt

Department of Atmospheric and Oceanic Sciences, University of Wisconsin, Madison

W. L. Ecklund, D. A. Carter, and J. S. Wilson

Aeronomy Laboratory, National Oceanic and Atmospheric Administration, Boulder, Colorado

Abstract. We present observations with a 915-MHz boundary layer profiler of reflective layers in the clear air that persist as light rain falls through them. In the three cases presented a clear-air echo is initially present over several hours and confined to a horizontal layer a few hundred meters thick. Subsequently, light rain falls through the layer but does not eliminate the spatial pattern of refractive index irregularities which presumably accounts for the clear-air echo. When the reflectivity of the rain is comparable with that of the clear air, Doppler spectra in the vertical profiler beam have separate modes arising from Rayleigh scattering by the rain and Bragg scattering by the clear air. The modes are distinguishable because of the fall velocity of the drops relative to the air. Using an algorithm to separate the clear air and precipitation components of these bimodal spectra, we can isolate the power and velocity of each mode. This allows us to see interactions of the two backscattering mechanisms. In one puzzling case the clear-air reflectivity in a layer increases by an order of magnitude as rain falls through it, but in the other cases no such strong effect occurs. We discuss possible causes of the increase in reflectivity but find no convincing explanation.

1. Introduction

Since May 1992, a 915-MHz boundary layer wind profiler has been operated in downtown Montreal as a collaborative project of the National Oceanic and Atmospheric Administration (NOAA) and McGill University. Rogers *et al.* [1994] have described the profiler and have given examples of data from the first year of operation. The profiler is fundamentally an improved version of the prototype model of the small UHF profiler described by Ecklund *et al.* [1988, 1990] and the profiler employed on the Hawaiian Rainband Project [Rogers *et al.*, 1993].

In light precipitation the profiler sometimes observes bimodal Doppler spectra, in which one mode arises from Rayleigh scattering by the raindrops or snowflakes and the other from Bragg scattering by refractive index fluctuations in the clear air. These are the kind of bimodal spectra that several re-

searchers have used for estimating the drop size distribution in rain [Wakasugi *et al.*, 1986; Gossard, 1988; Courrier, 1990; Rogers *et al.*, 1993]. The presence of distinguishable clear-air and rain modes in spectra measured in the vertical beam enables the measurement of drop fall speed relative to the air and hence of drop size. We have examined some of these observations from another point of view, to determine what effect, if any, the precipitation has on the scattering properties of the clear air. The mixing-in-gradient theory of Bragg scattering by the clear air leads us to believe that the reflectivity of the air may be influenced by the introduction of rain or snow. As recently reviewed by Gage [1990] and Gossard [1990], the theory has two main requirements: (1) the existence of a background or mean gradient of refractive index; and (2) the existence of some degree of turbulence to act on the mean gradient and create spatial irregularities with a scale of half the radar wavelength. In the lower atmosphere the necessary background gradients may be found in the boundary layer near the ground, at

Copyright 1995 by the American Geophysical Union.

Paper number 94RS03168.

0048-6604/95/94RS-03168\$08.00

inversion layers [Rogers *et al.*, 1993], or at cloud boundaries [Knight and Miller, 1993]. Usually it is the gradient of humidity, not temperature, that accounts for the spatial variability of the refractive index. Thus in the Hawaiian trade wind inversion, which provides a strong clear-air echo, it is the sharp decrease of dew point with altitude that creates the refractive index gradient. When rain or snow falls through a region of reflective clear air it modifies the humidity structure and possibly influences the small-scale air circulation and thus may affect the reflectivity.

We have examined our data for evidence of rain effects on clear-air echoes. The task is complicated by the fact that the echoes in the boundary layer and those associated with cumulus clouds are essentially created by convection and mixing and hence are highly variable in space and time. To attribute any observed changes in clear-air reflectivity to the appearance of precipitation in these situations seems risky. Therefore we have focused attention on the other kind of clear-air echoes, those in the form of persistent layers, which are probably accounted for by quasi-horizontal features such as inversions or elevated frontal surfaces.

This paper presents three examples of the interaction of rain with elevated reflective layers in the clear air. In each case the rain is light enough that the clear-air spectral components are still discernible in the Doppler spectra. These bimodal spectra were analyzed to determine the separate contributions of the raindrops and the clear air to the total target reflectivity. Also, the mean velocity and the velocity spread of the clear-air mode were analyzed to look for any effects of the rain. In these examples the clear-air reflective layers continue to exist in the presence of the rain. In one case the reflectivity of the layer actually increases by approximately 10 dB at just the time the rain reaches it. In the other two no such strong interaction is evident. Possible effects of rain on scattering by the clear air are discussed, and it is not clear to us, in terms of the generally accepted Bragg scattering theory, how rain can account for the observed increase in reflectivity.

2. Reflectivities of Rain and Clear Air

The McGill/NOAA profiler is capable of detecting very light rain and has about the same sensitivity to light rain as to moderately reflective clear air.

The reflectivities η_r of rain and η_a of the clear air are given by

$$\eta_r = 0.93 \pi^5 Z \lambda^{-4} \quad (1)$$

$$\eta_a = 0.38 C_n^2 \lambda^{-1/3} \quad (2)$$

where Z is the reflectivity factor of rain [Battan, 1973], C_n^2 is the structure parameter characterizing the strength of the fluctuations in the refractivity of the air [Gossard and Strauch, 1983], and λ is the radar wavelength. At the 0.33-m wavelength of the profiler the relation between the refractivity structure parameter and the rain reflectivity factor that produces the same reflectivity is

$$\log_{10} C_n^2 = \zeta/10 - 13.4 \quad (3)$$

where $\zeta = 10 \log_{10} Z$ is the reflectivity factor in units of dBZ. Thus a reflectivity factor of 0 dBZ corresponds to a structure parameter of $10^{-13.4} = 4 \times 10^{-14} \text{ m}^{-2/3}$, 10 dBZ corresponds to $4 \times 10^{-13} \text{ m}^{-2/3}$, and so forth. At a range of 2 km the profiler can detect clear air with C_n^2 of the order of $10^{-15} \text{ m}^{-2/3}$, corresponding to about -15 dBZ.

3. Observations

We present examples of elevated clear-air layers which persisted during light rain on three days: September 21 and 27, 1992, and June 20, 1993. The first of these days is the most puzzling because of large changes in the clear-air reflectivity that appear to be caused by the rain.

3.1. September 21, 1992

Figure 1 shows the radar reflectivity (expressed as rain-equivalent reflectivity factor in dBZ) and the mean Doppler velocity from 2 hours of observations (1600 to 1800 UTC) collected with the vertical beam of the profiler. Each vertical profile included in this contour plot comprises approximately 30 s of real-time integration, and there are 30-s gaps between each profile, during which time a measurement was made with an oblique beam. Our radar calibration assumes a constant noise temperature, and the calibration has been tested against a rain gauge. During the first hour there is a persistent reflective layer at 1.7 km with maximum reflectivities between about 5 and 15 dBZ and no significant vertical motion. In sections 4.1 and 5.1 we will show this layer to be explained by a strong humidity gradient. By 1700 UTC precipitation is visible aloft, and by

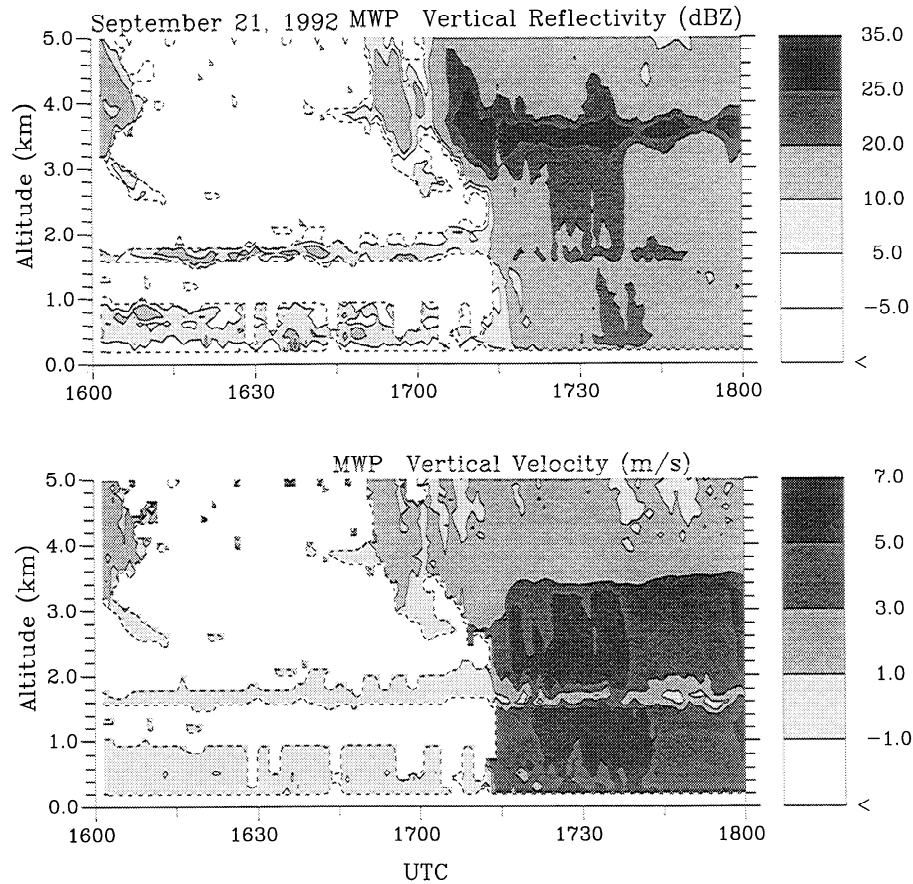


Figure 1. Time-height pattern of (upper) reflectivity and (lower) mean Doppler velocity in the vertical profiler beam from 1600 to 1800 UTC on September 21, 1992. The dashed contour defines a signal-noise ratio below which the signal is not plotted. Reflectivity intervals are selected to indicate significant features, and are not equal.

1715 the melting layer is apparent in both the reflectivity and vertical velocity near 3.6 km. Also by 1715 rain has fallen through the clear-air layer. During the rain the layer is no longer visible in the reflectivity plot but still shows in the velocity pattern because the clear-air mode in the bimodal spectra biases the mean Doppler velocity towards zero.

The procedure for separating and analyzing the two individual spectral modes is described in Appendix 1. Applying this procedure yields Figures 2 and 3. Figure 2 shows the reflectivity and fall speed of just the rain mode of the spectra. The fall speed now is a continuous field, uninterrupted by the clear-air layer at 1.7 km. Figure 3 shows the reflectivity and vertical motion of just the clear air. The vertical velocities are mostly within $\pm 0.5 \text{ m s}^{-1}$ and appear unaffected by the rain. The echoes below 1

km may be from the clear air but may also be from ground clutter. Located atop a tall building, the profiler suffers from ground clutter at ranges less than about 1 km. The clutter is centered at zero velocity in the Doppler spectrum and so may interfere with clear-air measurements at close ranges. Rain echoes do not have this problem because they are strong enough and have a large enough Doppler shift to be separable from the clutter.

The surprising feature of Figure 3 is that the clear-air reflectivity does not weaken as the rain begins, as we might expect if the humidity irregularities were smoothed out by evaporation of the rain, but actually strengthens by more than 10 dB. Beginning at 1715, exactly as the rain reaches 1.7 km, the clear-air reflectivity increases from just under 10 dBZ to nearly 20 dBZ. In sections 4 and 5 we will consider the cause

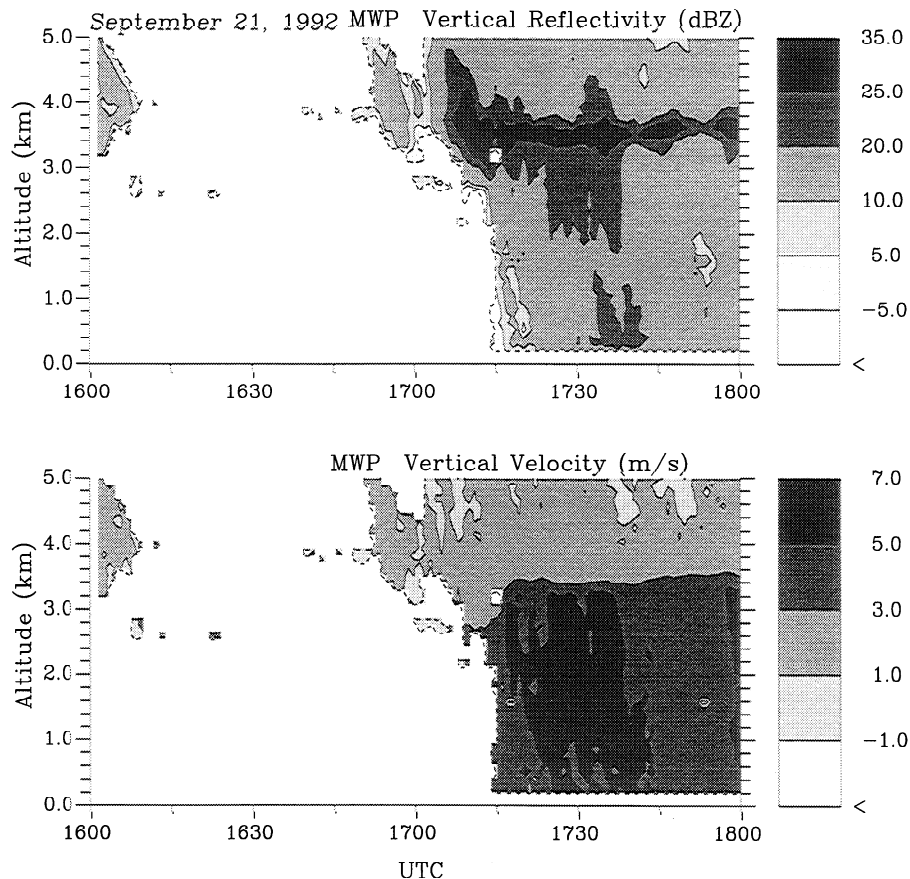


Figure 2. Time-height pattern of (upper) reflectivity and (lower) mean Doppler velocity attributed to the precipitation mode, for the same observations as in Figure 1.

of the layer and possible explanations of the increase in reflectivity coincident with the rain.

3.2. September 27, 1992

Figure 4 shows the reflectivity and mean Doppler velocity in the vertical beam from 3 hours of observations on September 27, 1992. A sloping reflective layer is seen at 2.3 km at 1330 UTC, descending to 1 km by 1530. Reflectivities in the layer are generally weaker than those in the first example. The Doppler velocities are less than 1 m s^{-1} , as expected of a clear-air echo. The synoptic context of this layer is discussed in section 4.2. Light rain falls through the layer beginning at about 1430 but apparently does not eliminate the refractive index gradients causing it. The reflectivity and fall speed of the rain are shown in Figure 5 and those of the clear air in Figure 6. Because the rain on this day is so light, sometimes with a mean fall speed less than 3 m s^{-1} , there are times when the separation

algorithm fails. Where gaps exist in the clear-air layer the reflectivity and velocity of the corresponding rain echo may be erroneous. This is because some Bragg-scattered power may be misidentified as coming from Rayleigh scatter. Similarly, where rain echoes are discontinuous, for example at 1443 UTC at 1.6 km, we must be suspicious of the clear-air result. An interesting feature of this case is the slight strengthening of the clear-air echo around 1445. While this is not as dramatic as the order-of-magnitude increase on September 21, it nevertheless appears to be associated with rain falling through the layer. However, there is no apparent strengthening of the clear-air echo at 1.2 km during the second shower at 1515.

3.3. June 20, 1993

On this day a clear-air layer first appeared at 1.4 km at 1600 UTC. Over the next 7 hours the layer gradually ascended to 1.8 km and then returned to

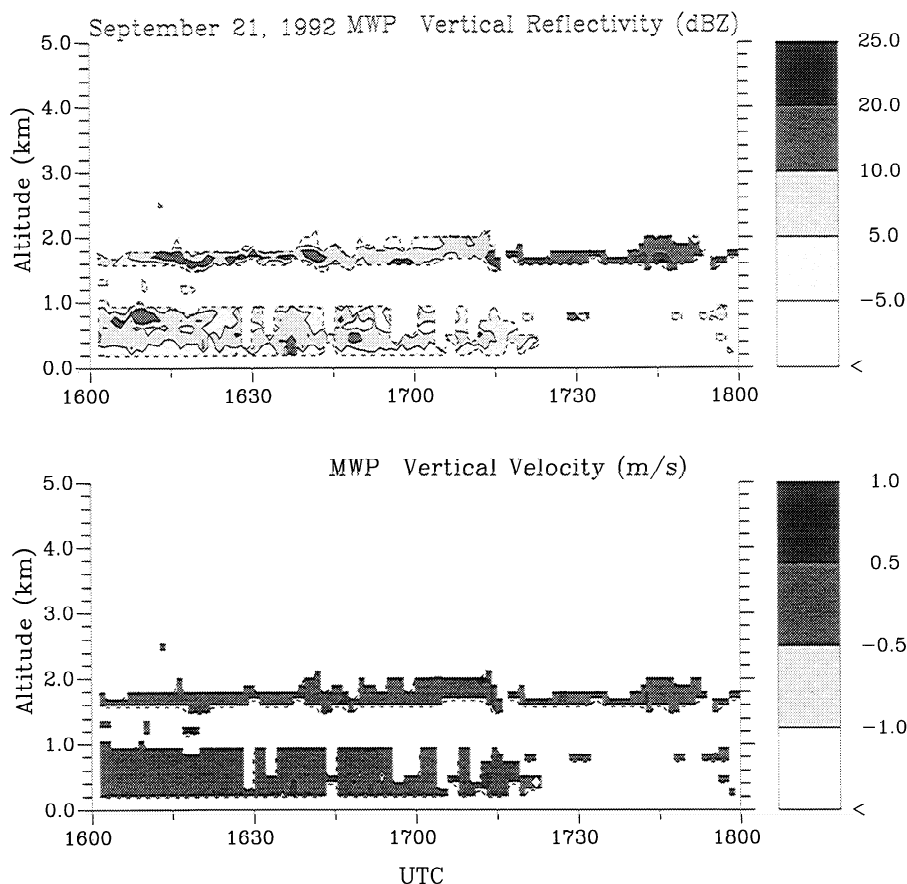


Figure 3. Time-height pattern of (upper) reflectivity and (lower) mean Doppler velocity attributed to the clear-air mode, for the same observations as in Figure 1. Velocity intervals are finer here to give better resolution of small changes.

1.4 km at 2300, after which it descended quickly below 1 km. Figure 7 shows the total reflectivity and vertical velocity for this period. The antenna cycle on this day consisted of five consecutive measurements with the vertical beam, followed by measurements with each of the four oblique beams, each measurement requiring approximately 30 s. Therefore the data contoured in Figure 7 consist of blocks of five 30-s measurements separated by 2-min gaps. The clear-air layer is most apparent in the velocity field. The reflectivity and mean Doppler velocity of the rain component are shown in Figure 8 and those of the clear air in Figure 9. Light, intermittent rain showers began at 1830 and became steadier at 2300. A melting layer was intermittently present after 1830 at 3.5 km, off the scale of these plots. In Figure 9 we see the layer of interest above 1 km, and another apparent clear-air layer at 0.8

km. This lower layer may be real, but it also may be affected by ground clutter, so we will not consider it in the analysis. In addition to its wandering altitude, interesting features of the upper layer are its slightly increased intensity soon after one of the first showers at 1930, and again at 2330 in the heavier rain.

On this day, unlike the earlier examples, a laser ceilometer was operating next to the radar. This instrument is intended to measure cloud base altitude, and it also detects moderate rain. The cloud base as determined by the ceilometer is plotted in Figure 10. It shows no clouds below 4 km until 2230. Between 2230 and 0030 (June 21) the cloud base is always above 2.5 km, remaining well above the clear-air layer. The low ceiling from 0030 onwards is associated with the light rain that was then reaching the ground. The ceilometer record confirms that at least on this day, the thin layer we

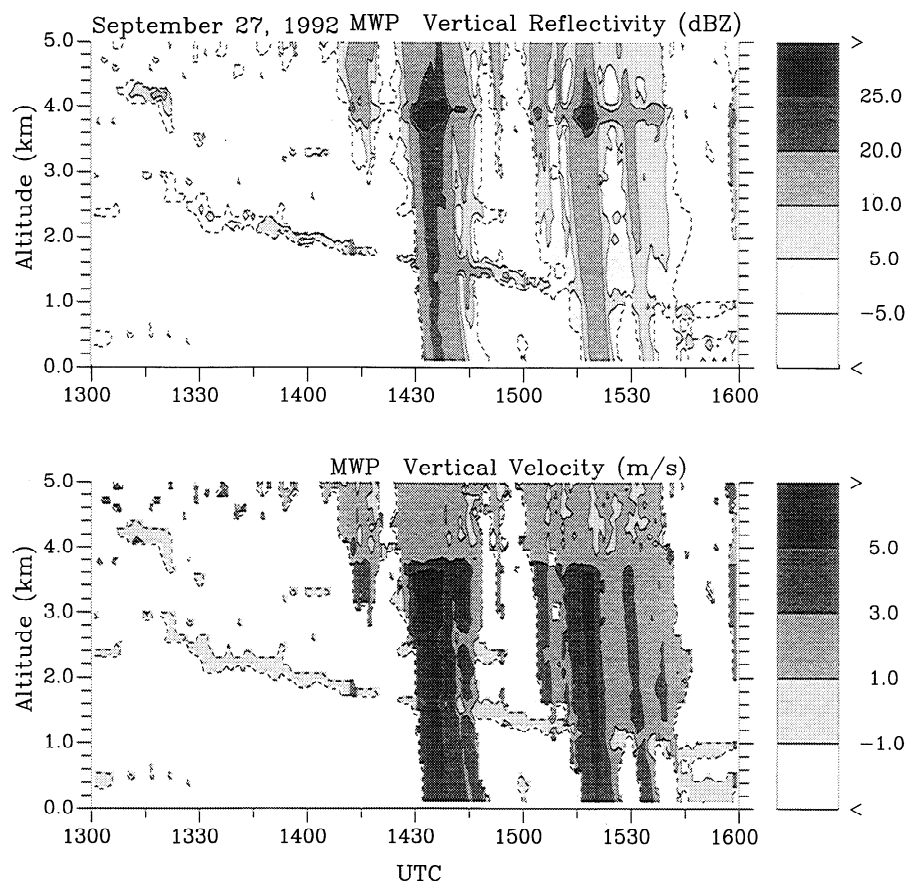


Figure 4. Time-height pattern of (upper) reflectivity and (lower) mean Doppler velocity in the vertical beam, from 1300 to 1600 UTC on September 27, 1992.

interpret as clear air cannot be explained by scattering from cloud droplets.

4. Synoptic Context

In section 5 we will argue that moisture gradients are the cause of these clear air layers. Here we present a brief synoptic overview and detailed moisture analysis for each case. Water vapor mixing ratio often has sharp gradients both in the vertical and horizontal, so it must be analyzed with care. We have created cross sections of the vertical gradient of mixing ratio using an analysis procedure described in Appendix 2. Weather data were objectively analyzed on isentropic surfaces using surface and radiosonde observations surrounding the times of the three cases.

Figure 11 shows the locations of the cross sections presented in this section. For the first two cases cross section A-B is used, and for the third we

will show a cross section at C-D. All three cases feature a deep moisture surge initially to the southwest of Montreal and eventually passing through the radar site. The cross sections are aligned with the wind in the moisture surge, so in a crude sense the time evolution at Montreal can be seen by looking along the cross section. For each case we show a cross section containing virtual isentropes (light contours at intervals of 2 K), mixing ratio (heavy contours at intervals of 1 g kg^{-1}), and the absolute value of the vertical gradient of mixing ratio (shaded areas). Air motion was generally from left to right in the moist layer, and all cases had little directional shear, though the wind direction did change with time by up to 45° over 24 hours.

4.1. September 21, 1992

On this day a deep surge of moisture from the Gulf of Mexico moved into the Great Lakes region, wedged between a departing surface high off the

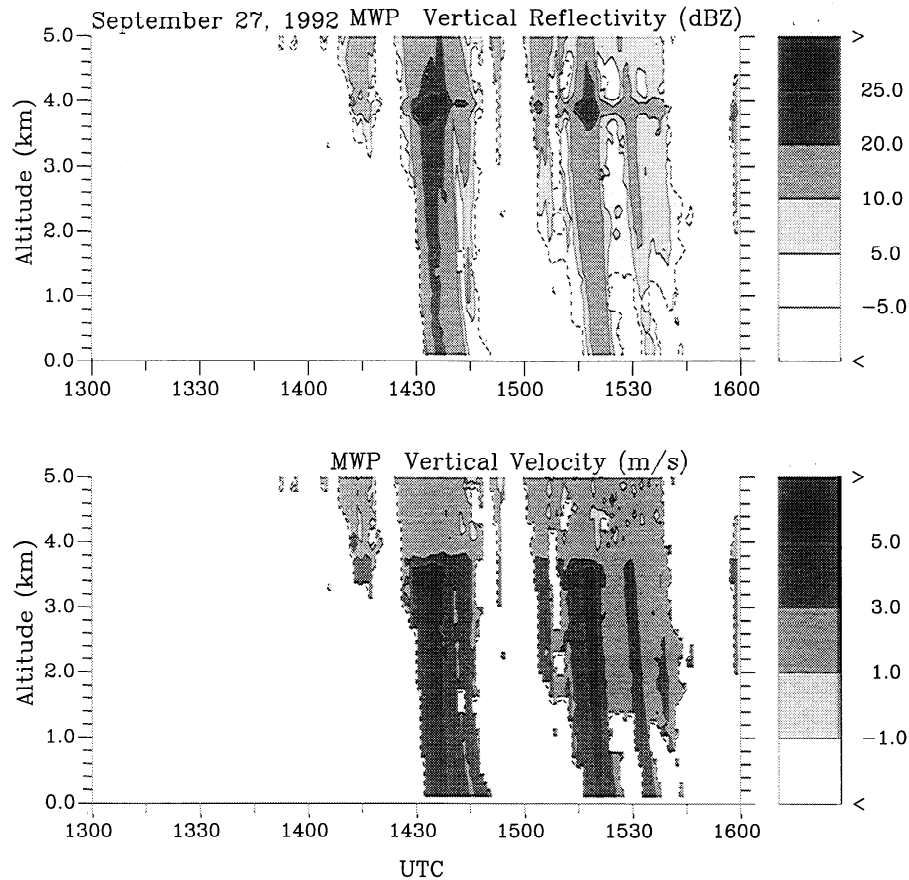


Figure 5. Time-height pattern of (upper) reflectivity and (lower) mean Doppler velocity attributed to the precipitation mode, for the same observations as in Figure 4.

coast of Maine and a deep, elongated, positively tilted trough over the Mississippi Valley. The surface high was shallow with westerly flow over the top. This flow advected dry low-level air from the north central Great Lakes area up the isentropes to 2–4 km over the St. Lawrence Valley by 1200 UTC on September 21. This created the moisture pattern shown by the shaded moisture gradient in Figure 12, with a shallow moist layer over the radar site and deep moisture upstream. The sloping isentropes upstream of Montreal indicate a warm front. The entire pattern coherently advected to the northeast, with deep moisture having reached Montreal by 0000 UTC on September 22, and the tight vertical moisture gradient of nearly identical shape located downstream.

The clear-air radar echoes (Figure 3) persisting at 1.7 km coincide with the region of strong vertical moisture gradient. The peak intensity of this mois-

ture gradient at 1200 UTC occurs some further distance upstream, and the gradient is still seen in an analysis 12 hours later, after having passed through Montreal. This strong gradient results from the inflow of moisture in the lowest 1 km while the layer above remains dry. This vertical moisture gradient was captured well in the Albany and Buffalo soundings located a short distance on either side of the cross section and reproduced in the analysis. This can explain clear-air returns increasing in magnitude during the morning but cannot explain the sudden increase upon onset of the rain, since rain falling from above the dry layer could not preferentially moisten the already moist lower layer.

A low-level jet analyzed at 22 m s^{-1} and 1.7 km propagated to the northeast just behind the region of frontal upglide. Bulk Richardson numbers at the base of the jet were near, and in some places below,

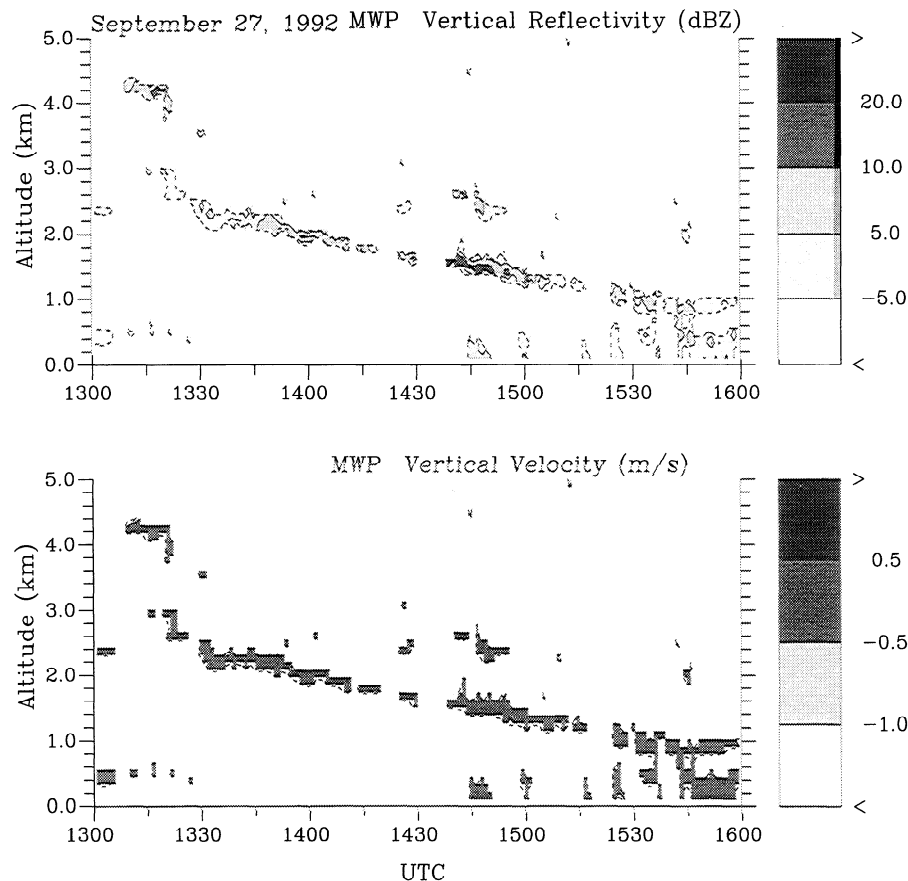


Figure 6. Time-height pattern of (upper) reflectivity and (lower) mean Doppler velocity attributed to the clear-air mode, for the same observations as in Figure 4.

1.0, though nowhere below 0.25. However, this jet did not appear to have reached Montreal until at least 7 hours after the layer was seen to intensify, so associated turbulence cannot explain the increase in clear-air echo intensity.

4.2. September 27, 1992

On this day a deep layer of moist air, again originating over the Gulf of Mexico, surged ahead of a strong, negatively tilted, diffluent short wave. The wave was moving from over the Great Lakes into the longwave ridge position over eastern Canada. Extremely dry air under the ridge axis had already pushed well beyond the radar site before the observation period of Figure 4. Embedded within the moist air was a dry layer created by midlevel subsidence in the right exit region of a midlevel jet streak associated with the short wave. The base of this dry layer formed the moderately strong moisture gradient showing up in the cross

section of Figure 13. The analysis appears to show this relatively dry air originating from midlevels, but it is not clear how it was able to descend as far as it did. The 1200 UTC analysis of Figure 13 shows this strong gradient at about 2.5 km, which is slightly below the height of the clear-air layer seen over Montreal beginning about 1 hour later. The analysis gives no indication that this layer should be sinking down to 1 km, as is seen in the radar echo; however, the situation by the next analysis time, 0000 UTC (September 28), has changed considerably as the short wave rotated through. One possible explanation for the descent of the reflective layer is as follows: The wind speed associated with the wave increased during the 24-hour period surrounding these observations, and Montreal remained near the jet streak exit region for some hours after 1200 UTC, so dynamic forcing could conceivably have generated subsidence to lower

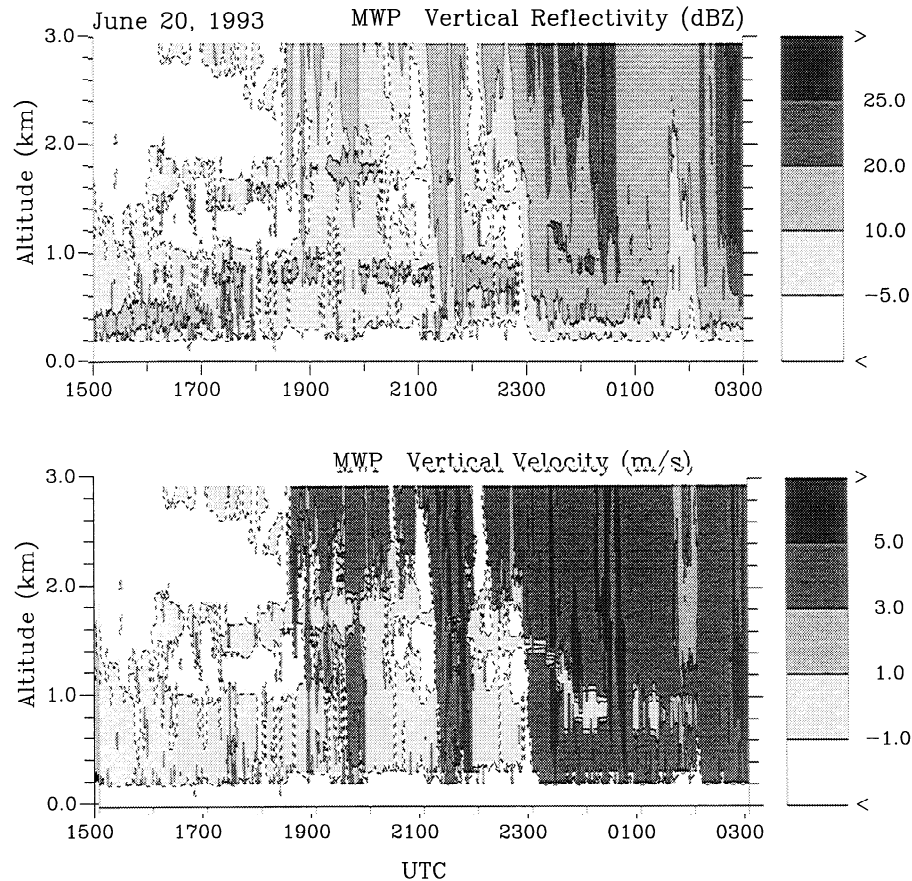


Figure 7. Time-height pattern of (upper) reflectivity and (lower) mean Doppler velocity in the vertical beam, from 1500 to 0300 UTC on June 20 and 21, 1993. Data from only the lowest 3 km are plotted.

altitudes over time. Then, vertical advection would have lowered the top of the less moist layer, thereby lowering the altitude of the moisture gradient.

4.3. June 20, 1993

On this day the pattern of moisture over Montreal was influenced both by synoptic features over the Canadian Maritime provinces to the east and by features over the midwestern United States.

Confluent northwesterly flow aloft behind a strong wave exiting the Canadian Maritimes created strong midlevel subsidence. Between 0000 UTC and 1200 UTC on June 20 dry midlevel air in this northwest flow was advected downward, creating a strong moisture gradient close to the surface. At 1200 UTC a strong maximum in this vertical moisture gradient was just upstream of Montreal at 1.5 km, where lingering low-level moisture remained

beneath the dry subsiding midlevel air. At the same time, a strong wave over the Midwest was pushing a warm front and moisture surge northeast toward the eastern Great Lakes and the St. Lawrence Valley.

During the day, rain moved into the Montreal region. To the northeast temperatures rose under clear skies, which, combined with cold air aloft, created unstable conditions resulting in a deep surface-based mixed layer entraining the dry air above. The remains of the afternoon deep mixed layer can be seen in the 0000 UTC cross section (Figure 14) as the region of exceptionally weak vertical gradient in potential temperature northeast of Montreal. A rain-cooled cold pool sat above Montreal, and the warm front overrode this cold air, following upward-sloping isentropes. The cold pool was a regional phenomena, extending from

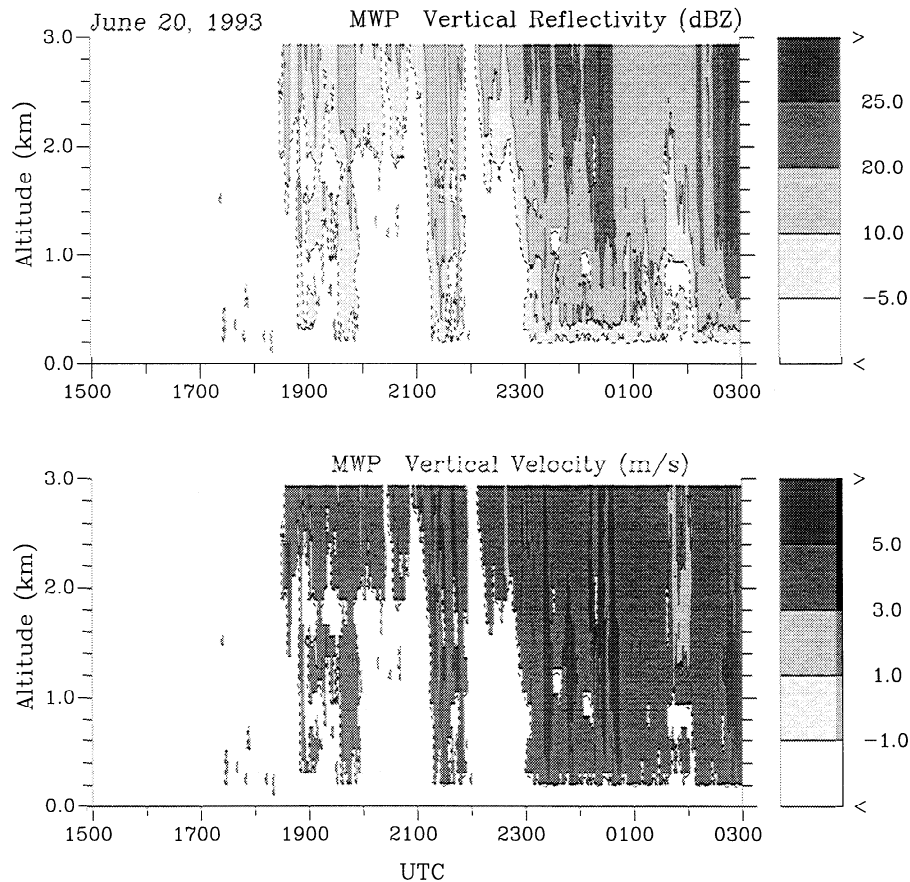


Figure 8. Time-height pattern of (upper) reflectivity and (lower) mean Doppler velocity attributed to the precipitation mode, for the same observations as in Figure 7.

Massachusetts to southeastern Ontario at 1800 UTC. This pattern created a bulge in the isentropes, and the pattern of moisture gradients flowed up over the cold dome. As the cold pool moved over Montreal, the thickness of cold dry air above the radar site increased, so the moisture gradients appeared at higher altitudes. This is consistent with the ascending clear-air returns in Figure 9. However, by 0000 UTC June 21 the analysis (Figure 14) shows the greatest depth of the cold pool over Montreal and the low-level moisture gradients having weakened. One feature that this moisture analysis is not able to explain is the lowering of the reflective layer and the strong returns in the evening hours. That abrupt lowering coincides with the beginning of a period of steady rain (Figure 8) and its cause is no better understood than the strengthening of the clear-air layer during the September 21, 1992, example.

5. Discussion

The moisture gradients shown in the synoptic analysis point to Bragg scatter as the explanation of the persistent reflective layers. We will next consider to what extent the radar observations agree with this interpretation. Finally, we will consider how precipitation may affect the clear-air scattering mechanism.

5.1. Cause of the Reflective Layers

The reflectivity, vertical motion, and limited vertical extent of the observed layers all suggest Bragg scattering. Typical reflectivities before interaction with rain are less than 10 dBZ corresponding to C_n^2 of at most a few times $10^{-13} \text{ m}^{-2/3}$. Clear-air echoes of this strength are often observed in the lower troposphere [Chadwick and Moran, 1980; Knight and Miller, 1993; Rogers et al., 1993]. The thin layer in each case is consistent with clear-air reflec-

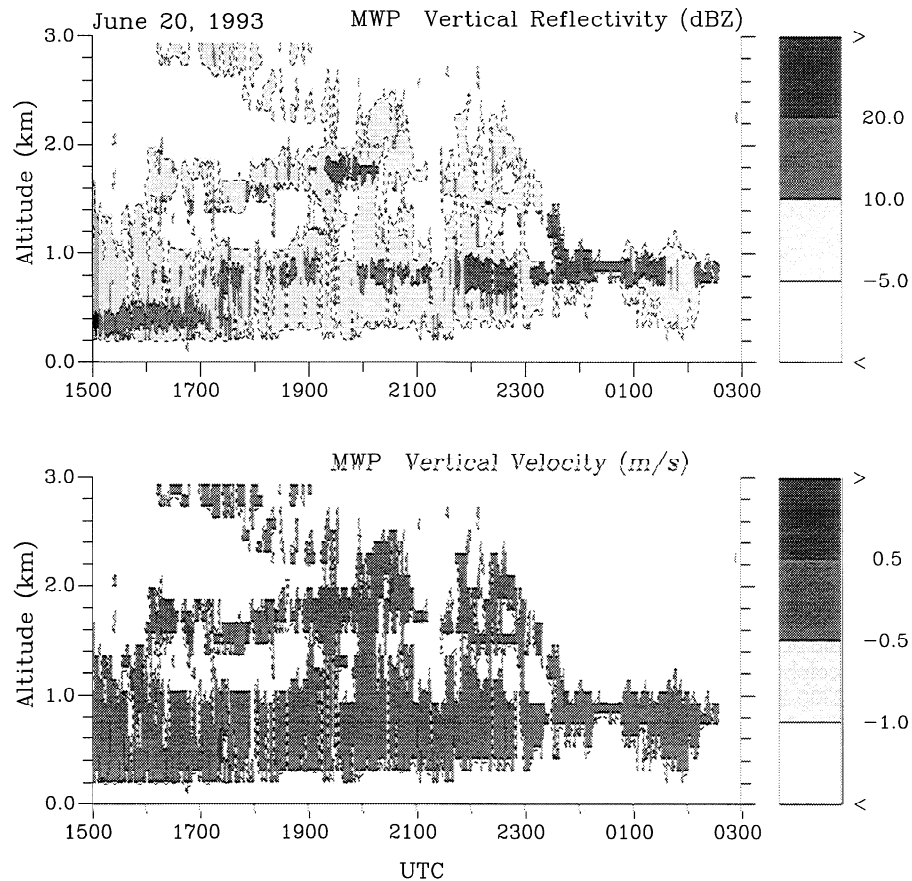


Figure 9. Time-height pattern of (upper) reflectivity and (lower) mean Doppler velocity attributed to the clear-air mode, for the same observations as in Figure 7.

tion at a strong humidity gradient, and humidity gradients are seen in the synoptic analysis of section 4. A temperature profile on September 21, 1992, measured at the nearest radiosonde station (Maniwaki, Quebec) is shown in Figure 15. Although this sounding is 5 hours earlier than the radar observations and 250 km away, it shows a strong decrease of dew point with altitude at 1.4 km. We believe this dry layer was present over Montreal at 1.7 km and was responsible for our observations. Winds measured with the profiler at 1745 UTC are at the right of the Figure. Dry layers resembling this one were present on the two other days considered, and it is likely that similar humidity gradients are responsible for most persistent thin layers observed by boundary layer profilers.

We can further argue that the reflective layers do not result from Rayleigh scattering from cloud or drizzle drops. The reflectivity of a cloud depends on

drop size and concentration. To account for echoes with a reflectivity factor of 10 dBZ by cloud droplets, consider droplets of 40 μm in diameter. These are large for cloud droplets, but have a terminal fall speed of only about 6 cm s^{-1} , and so are not distinguishable from clear air in the Doppler spectrum. The reflectivity would require a concentration of 2500 drops per cm^3 , much larger than ever observed, and would also imply an entirely unrealistic cloud water content. If not cloud droplets, then could drizzle drops explain the layer echo prior to the rain? Drizzle drops are about 0.1 mm in diameter and have a terminal velocity of 0.3 m s^{-1} , which might not be distinguishable from clear air. The observed reflectivities of 10 dBZ and greater would require at least 10 of the 0.1-mm drops per cm^3 , and thus liquid water contents of more than 5 g m^{-3} : values that are too large. Larger drizzle drops, with a 0.2-mm diameter, would account for

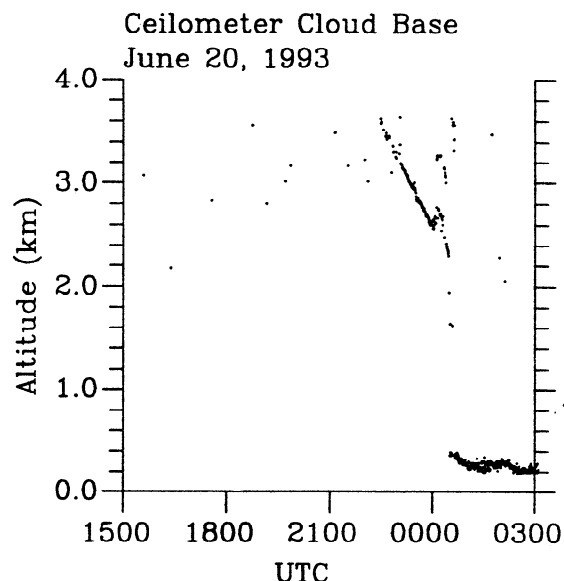


Figure 10. Altitude of cloud base measured by the laser ceilometer during the time of the observations in Figure 7. The Figure shows a precipitating cloud base descending through 3 km between 2300 and 0030. Beginning at 0030 a lower cloud deck associated with heavier rain is present.

10 dBZ with a water content of only 0.7 g m^{-3} , a value close to being acceptable, but would fall at nearly 0.8 m s^{-1} and would thus be recognizable in the radar data as having an average displacement from zero velocity over time. Moreover, neither cloud nor drizzle seems a likely explanation of the reflective layers because the layers are so thin. We conclude that Bragg scattering by the clear air is the more likely explanation.

5.2. Strengthening of the Reflective Layer on September 21

Figure 16 shows the evolution of the Doppler spectra at three altitudes: above the clear-air layer (2.1 km), at the center of the layer (1.7 km), and just below the layer (1.5 km). Spectra are shown over five profiles (30-s integrations) taken 1 min apart. The vertical lines indicate zero Doppler shift, and each spectrum extends from -10 m s^{-1} to $+10 \text{ m s}^{-1}$. If present, clear-air modes are expected to be close to zero Doppler shift, and rain modes are expected to be shifted to the right of zero, indicating downward motion. In Figure 16a each spectrum is normalized in the sense that the maximum spectral amplitude is plotted full-scale. At 2.1 km we first see only a very weak clear-air echo at 1313. By 1714

rain has reached this altitude. In the center of the layer, at 1.7 km, we see the clear-air echo for the entire time. The rain echo is visible beginning at 1715, but is considerably weaker than the clear-air echo. Below the layer there is no signal at all before 1715, when the rain mode appears. A clear-air mode becomes visible at this altitude beginning at 1716. Figure 16b shows the spectra plotted to the same amplitude scale. As we observe the clear-air mode at 1.7 km over time, we can see its intensity increase dramatically at 1715, exactly when the rain first reached this altitude. At 1.5 km the clear-air mode appears at 1716, 1 min after the rain.

Spatial irregularities in the refractivity are caused by turbulence acting on mean gradients of the potential refractive index [Tatarski, 1961]. Because vertical gradients of potential refractive index are generally much stronger than those in the horizontal, a common model is to consider this vertical gradient as it is mixed by turbulent eddies. The turbulence brings together air with different values of refractivity, creating the spatial fluctuations necessary for clear-air echoes. The structure parameter C_n^2 measures the strength of these irregularities and may be shown to depend on the vertical gradient of

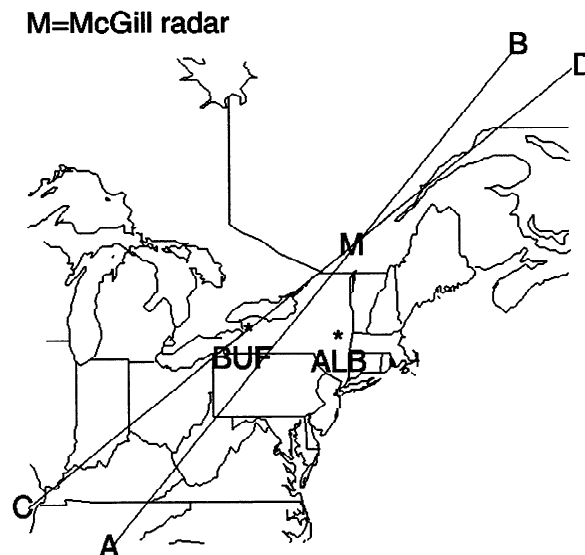


Figure 11. Location of cross sections shown in Figures 12–14. The Albany, New York (ALB), and Buffalo, New York (BUF), sounding positions are shown, as is the location of the McGill/NOAA wind profiler (M). Cross section A-B was used for Figures 12 and 13, and C-D was used for Figure 14.

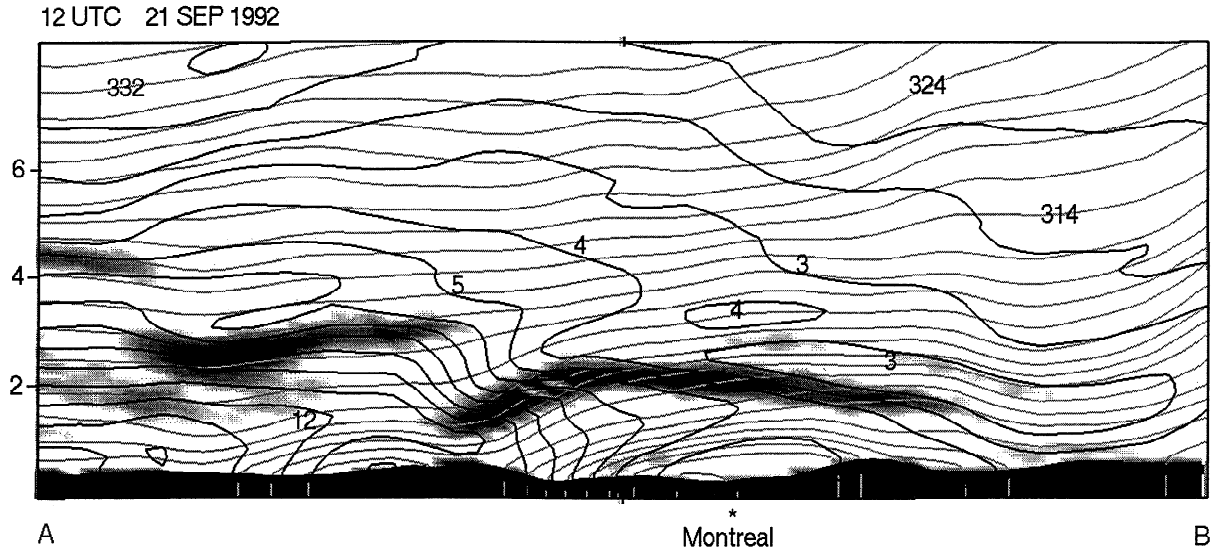


Figure 12. Cross section along A-B showing the pattern of moisture at 1200 UTC September 21, 1992. Vertical gradient of mixing ratio greater than $3 \text{ g kg}^{-1} \text{ km}^{-1}$ is shaded (3–5 gray, 5–7 black, >7 white inside black). Dark contours are mixing ratio (1 g kg^{-1} intervals); light contours are virtual potential temperature (2-K intervals). The vertical axis ranges from -0.8 to 8.3 km above sea level with 2, 4, and 6 km indicated on the left and underground regions shaded black. The location of the wind profiler (Montreal) is indicated.

potential refractive index and the intensity of the turbulence through the relation

$$C_n^2 = a^2 M^2 L_0^{4/3}$$

(4)

where L_0 is the outer scale of turbulence, M is the vertical gradient of the mean potential refractive index, and $a^2 \approx 2.8$ [Gage, 1990]. Rain could conceivably affect C_n^2 either thermodynamically

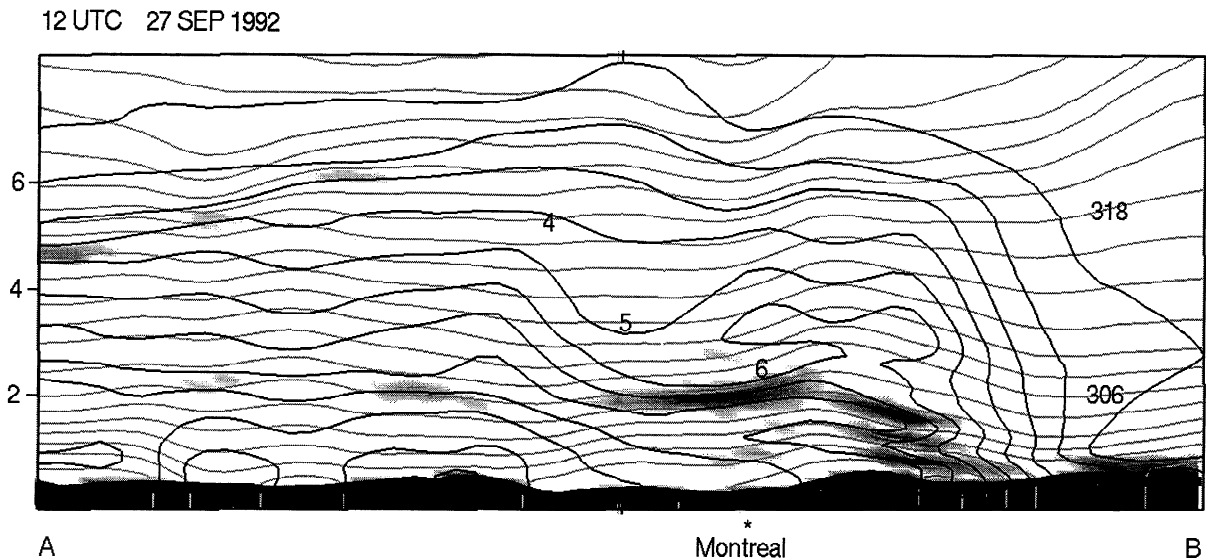


Figure 13. Cross section along A-B showing the pattern of moisture at 1200 UTC September 27, 1992. Contours and shading are as in Figure 12.

00 UTC 21 JUN 1993

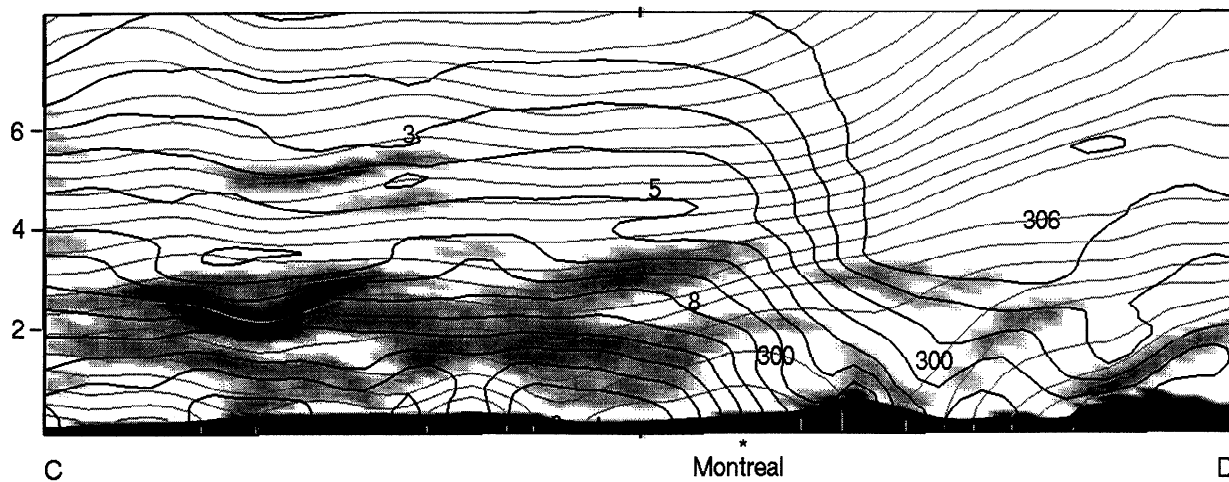


Figure 14. Cross section along C-D showing the pattern of moisture at 0000 UTC June 21, 1992. Contours and shading are as in Figure 12, except that shading is gray for 2–4 and black for 4–6 $\text{g kg}^{-1} \text{km}^{-1}$.

through the parameter M , or dynamically through L_0 . M depends on the vertical gradients of temperature and specific humidity and, for subsaturated air, may be written [Ottersten, 1969]

$$M = 77.6 \times 10^{-6} (p/T^2) \{ 7.73 (\partial Q / \partial z) - (\Gamma - \gamma) \cdot [1 + 15.46 (Q/T)] \} \quad (5)$$

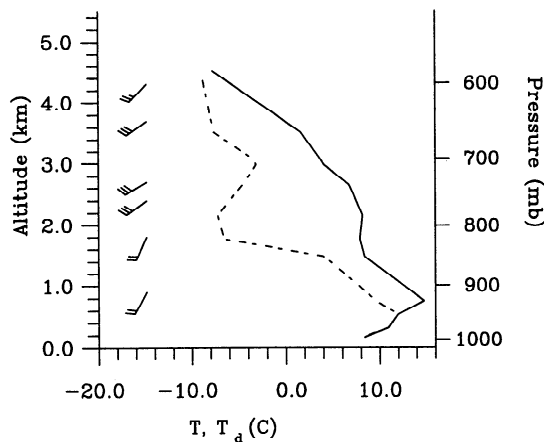


Figure 15. Maniwaki, Quebec, radiosonde (1200 UTC) showing temperature (solid curve), dew point (dashed curve), and wind (arrows on left) on September 21, 1992. The wind profile to the right was measured with the profiler at 1745 UTC. Winds are plotted in knots. Each full line on the tail of a wind arrow represents 10 knots, and a half line, 5 knots.

where p denotes the pressure in millibars, T the temperature in K, Q the specific humidity in grams per kilogram, Γ the dry adiabatic lapse rate in K m^{-1} , and $\gamma = -\partial T / \partial z$ the ambient lapse rate. This equation is appropriate for subsaturated air because it assumes that when a parcel of air is displaced vertically its potential temperature and specific humidity are conserved. For a cloud-filled, saturated environment the wet bulb potential temperature is conserved and the specific humidity at every height is the saturation value. The expression for M appropriate for these conditions is [Rogers *et al.*, 1994]

$$M = (77.6 \times 10^{-6} / T^2) \{ [p + 9620 (e_s / T)] (\Gamma_s - \gamma) + 2.61 \times 10^7 \gamma [(e_s / T^2)] \} \quad (6)$$

where Γ_s is the saturated adiabatic lapse rate and $e_s = e_s(T)$ is the saturation vapor pressure in millibars. The drops themselves affect the refractivity of the cloudy medium, but from the results of Flock *et al.* [1982], the contribution of the drops is negligible compared to that of the other terms in (6) at a frequency of 1 GHz and for the weak reflectivities we observed. For the observations of September 21, (5) applies prior to the rain and probably also afterwards because the rain was so light. However, the tendency will be to move towards the value of M for saturated conditions.

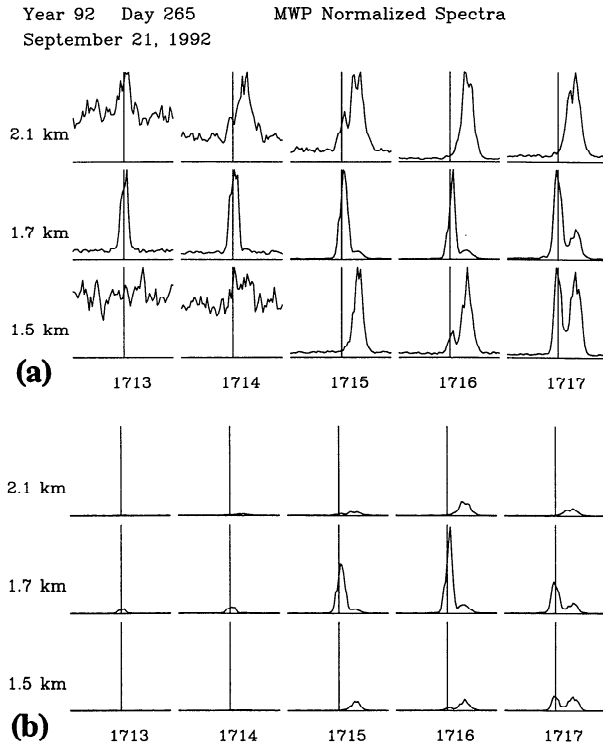


Figure 16. Raw Doppler spectra at three altitudes from 1713 to 1717 UTC on September 21, 1992, showing the increase in clear-air reflectivity as rain appears. The vertical line is at zero velocity, and the spectra extend from -10 m s^{-1} to $+10 \text{ m s}^{-1}$. The mode near zero velocity is due to clear air, and the faster velocity mode is from rain. (a) Spectra normalized to maximum amplitude to show the relative contribution of clear air and rain. (b) Spectra without normalization showing the change in reflectivity over time. See text for more details.

The other factor in (4), the outer scale L_0 , is related to the intensity of the turbulence by

$$L_0^{4/3} \propto \beta^{-2} \varepsilon^{2/3} \quad (7)$$

where $\beta = \partial v / \partial z$ is the mean wind shear and ε is the turbulent energy dissipation rate. This relation, given by *Hocking* [1985] and from equations 3.28 and 3.31 in *Tatarski* [1961], is appropriate for shear-driven turbulence in stably stratified air.

Consider now the possible effects of rain on the parameter M . The sounding on the day of these observations (Figure 15) shows an elevated inversion layer with a base at 850 mbar. Between 850 and 820 mbar the dew point decreases abruptly from 4°C to -7°C and the temperature is essentially isothermal at 7.5°C . Within this approximately 250-m thick

layer the refractive index decreases with height and M has its largest (absolute) value which, from (5), equals approximately $8.5 \times 10^{-8} \text{ m}^{-1}$. Accounted for almost entirely by the humidity gradient ($\partial Q / \partial z$) term, this is a large value and is consistent qualitatively with the high value of C_n^2 that we inferred from the reflective layer at 1.7 km. The most plausible effect of rain on the layer would be to increase the vapor content at the driest levels, where evaporation would be strongest, and to chill the air at these levels. In the limit the air would be cooled to the wet bulb temperature and would be saturated. For the thin layer in this example, the absolute value of M would be reduced to $5 \times 10^{-8} \text{ m}^{-1}$ by this thermodynamic change. If there were no other changes, the reflectivity from (4) would be reduced by a factor 0.6^2 , or 5 dB, contrary to what is observed. Even if evaporation were incomplete, and the wet bulb temperature were not reached, the effect would be to smooth out the humidity gradient and reduce $|M|$ somewhat. Actually, evaporation of the kind postulated would destabilize the initially isothermal layer because it would preferentially chill the top of the layer, where the air is initially driest. If the destabilization promotes vertical mixing, the gradients of humidity and temperature will be further reduced and the value of $|M|$, now given essentially by (6), will be lowered to approximately 10^{-8} m^{-1} . We conclude that the thermodynamic effect of rain on an air layer that is reflective because of a sharp refractive index gradient will be to reduce the reflectivity.

It is more difficult to speculate about possible dynamic effects of rain on the parameter L_0 . The destabilizing effect of rain evaporation, just mentioned, could increase the turbulent mixing in the layer, and hence the value of ε . This effect should also show up in the data as an increase in the spread of the clear-air spectral mode when the rain starts. We have used the Gaussian fit separation process described in Appendix 1 to estimate this spread for the layer at 1.7 km. The spectral width and its time variability do increase slightly after 1715 when the rain begins, but the average increase is only about 0.2 m s^{-1} , amounting to less than 20%, and cannot explain the increased reflectivity. Each falling drop also has a turbulent wake, but it seems unlikely that such fine scale and short-lived irregularities, even from an array of such drops, could contribute significantly to ε and the reflectivity. Finally, it is conceivable that rain falling through a layer with

wind shear might reduce the shear (β in (7)) a small amount because of the inertia of the drops and their exchange of momentum with the air, but this effect is thought to be too small to account for a significant increase in reflectivity. In short, we are not able to explain the increase in layer reflectivity by Bragg scattering using the ordinary and generally accepted considerations of a vertical refractive index gradient mixed by turbulence. The effect of rain would evidently be a reduction in reflectivity caused by a smoothing of the humidity gradients.

Rayleigh scattering, too, seems an unlikely explanation for echo intensification, for the same reasons that it would not explain the presence of the layer before the rain. The clear-air mode shows no significant fall speed, and cloud or drizzle drops necessary to produce the observed reflectivity and fall speed would imply too large a liquid water content. Furthermore, on June 20, 1993, the day ceilometer data were available, the cloud base was above the height of the clear-air layer.

5.3. Further Comments on Layer Strengthening

Several other ways by which the reflectivity of a thin layer might be increased by the occurrence of precipitation may be postulated. We have no evidence for these but present them only as speculation in the absence of convincing alternatives. The model on which (4) is based assumes only vertical gradients of refractive index. Horizontal gradients mixed by eddies would be equally effective in creating Bragg echoes, but this prompts the question of how they would form and why they would persist. One explanation for horizontal gradients is evaporation of raindrops as they fall into dry air. The drops could leave a trail of humid air that would mix with drier ambient air to create Bragg-reflective regions. Although this mechanism would explain how rain could cause increased reflectivity, it seems unlikely that it would be effective as quickly as the observations indicate. Moreover, there is no reason why this mechanism should affect only a narrow layer, as observed on September 21. If only evaporation is required, then the entire dry layer between 1.5 and 3.0 km should have had an increase in reflectivity.

Another possibility is what we might call Bragg scattering by raindrops. Bragg scattering is caused by spatial irregularities at a scale of half the radar wavelength so that echoes reinforce each other.

Smith [1964] and *Gossard* [1979] have considered the possibility that scattering by cloud droplets, because of their high concentration, may have a coherent or Bragg-type component. For our observations we do not believe cloud droplets were present in the reflective layer, but suggest that small raindrops falling through a turbulent field might show an increase in reflectivity due to a coherent component. As the drops fall their spatial distribution could conceivably be organized by the turbulent eddies to produce a Bragg scattering component. The drops act as tracers of the eddies, mimicking the refractive index structure and possibly enhancing the echo. In this way the combination of rain and the existing turbulent layer could produce the echoes we observe. There would be no "clear-air" peak above the turbulent layer because the small drops would not be coherently organized; the strengthening would occur just where the rain reaches the turbulent layer. This possibility is only speculative, and is not well-supported by the observations, which suggest that the layer that exists prior to the rain is explained by a strong background gradient of humidity, not by particularly intense turbulence.

6. Conclusion

We have shown three examples of observations in which light rain falls through thin clear-air reflective layers and the layers persist. Sometimes the reflectivity of the layer even increases during the rain, in one case by an order of magnitude. Evidence from synoptic analysis and radiosondes supports the conclusion that these layers are explained by Bragg scattering from the clear air, with refractivity gradients present because of a change of humidity with altitude. A convincing explanation for the increase in layer reflectivity coincident with the onset of rain has eluded us. Modification of the humidity profile by rain in processes considered likely would evidently tend to reduce the refractive index gradient and therefore the echo strength. We find no evidence for either a significant increase in turbulence intensity or for Rayleigh scattering by drops to explain the stronger clear-air echo. Something beyond the ordinary understanding of Bragg or Rayleigh scattering seems necessary to explain the observations.

Appendix 1: Separation of Clear-Air and Rain Echoes

Figure A1 shows a spectrum containing two distinct modes, from clear air and rain. This spectrum, and all those presented in detail in this paper, were taken at vertical incidence. Therefore, the mean Doppler shift of the clear-air echo indicates vertical air motion, and the Doppler velocities of the rain echo indicate drop fallspeed relative to the ground. The left mode, centered near 0 m s^{-1} , is the clear-air echo, while the mode on the right is due to raindrops. We wish to separate these modes and find the reflectivity, mean velocity, and spectral width associated with each. Two algorithms have been developed to do this automatically. The first assumes that the minimum point between the two modes represents a boundary between the spectra. Figure A2 shows the result of the separation. The light-shaded region is area associated with the clear-air echo, and the darker area is the rain echo. At the bottom, the unshaded area is system noise. The noise level of each spectrum is determined by the method described by *Hildebrand and Sekhon* [1974] and is available from the real-time radar processing. The first three moments of each shaded area are

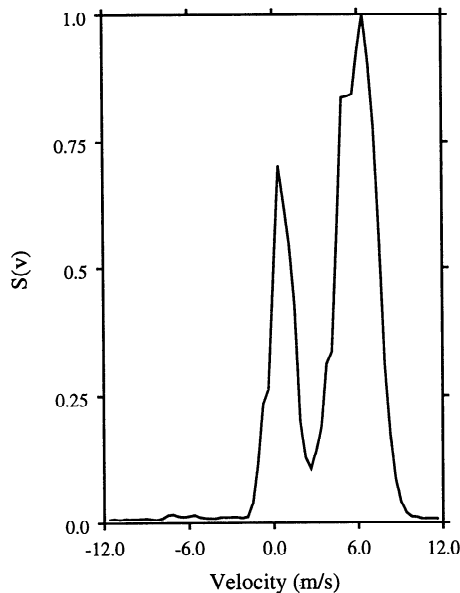


Figure A1. Sample bimodal Doppler spectrum measured on September 21, 1992 at 1.7 km. The left peak is the clear-air mode, with small vertical velocity. The right peak is the rain mode with a mean fall speed of about 6 m s^{-1} .

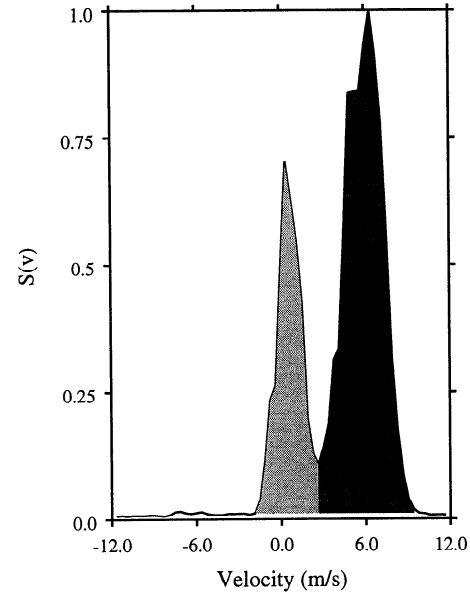


Figure A2. The same spectrum as in Figure A1, demonstrating the first separation method. The lighter shading is spectral content attributed to the clear-air mode, and the darker shading is the rain mode. The unshaded region at the bottom is below the spectrum noise level.

used to estimate the reflectivity, Doppler velocity, and spectral width of each mode. The spectra of the two modes will partially overlap, so by this method some power from each mode will be incorrectly assigned to the other. When the echoes are of similar magnitude this will have only a small effect on the reflectivity assigned to each mode. However, the overlap artificially narrows the calculated spectral widths. The advantages of this procedure are its simplicity and reliability. We use it for separation when we do not need to know the spectral width.

The second separation procedure is to fit the sum of two Gaussian functions, plus an offset for background noise level, to the spectrum. The form of the fit function $S(v)$ is

$$S(v) = N + A_a \exp \left[-(v - v_a)^2 / \sigma_a^2 \right] + A_r \cdot \exp \left[-(v - v_r)^2 / \sigma_r^2 \right] \quad (\text{A1})$$

where N is the noise level, A_a , v_a , and σ_a are the amplitude, mean velocity, and standard deviation of the clear-air mode, respectively, and A_r , v_r , and σ_r refer to those of the rain mode. Figure A3 shows the fit (dashed line) and the original spectrum (solid line). The Gaussian functions representing the two

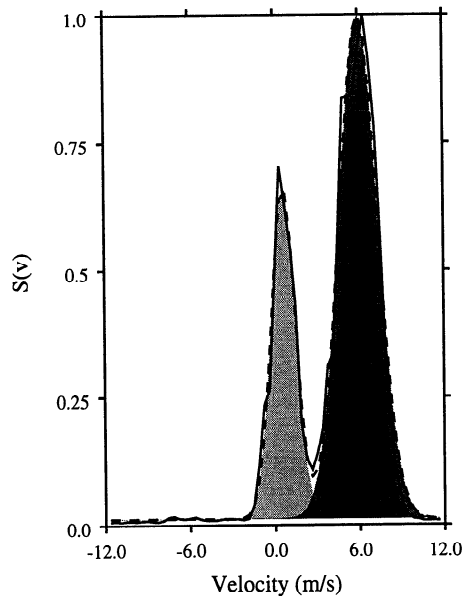


Figure A3. The same spectrum as in Figure A1 (solid curve), demonstrating separation by Gaussian fit. The dashed line indicates the best fit with two Gaussians. Light shading is the clear-air mode, medium shading represents the rain mode, and the darkest shade is the region common to both modes.

echoes are shaded, with the darkest shading where they overlap. This procedure explicitly provides an estimate of spectral width. Also, it has the advantage of properly separating the power from modes of different amplitudes. However, if the amplitudes differ by more than about one order of magnitude the fitting procedure will fail to recognize the weaker echo.

The data also contain many spectra with only a single peak. In that case we must decide if the echo is from clear air or rain. This is done based on the mean fallspeed and power of the echo. Processing to separate the echoes is automated but several parameters must be tuned for different conditions. Final corrections to the assignment of a single spectrum as clear air or rain are made by hand.

Appendix 2: Objective Analysis Procedure

Objective analysis used to create cross sections presented in section 4 began by interpolating the NCAR 2.5 degree gridded data set onto a 0.5 degree grid, and correcting to surface and radiosonde ob-

servations with a Barnes analysis [Barnes, 1973] applied to the discrepancies between observed and gridded data. These data were passed through a σ - z coordinate model to a visualization program (Vis-5D) [Hibbard *et al.*, 1994] which may be used to generate cross sections along any horizontal line. The Barnes analysis was applied to surface data using a Barnes radius of twice the observation spacing to avoid aliasing [Pauley and Wu, 1990]. A similar Barnes analysis was applied aloft on isentropic surfaces at 1-K intervals using both radiosonde data and the surface analyzed variables where the isentrope intersected the ground. Because mixing ratio is a nearly conserved quantity except near the boundary layer or precipitation, it tends to advect long distances in isentropic layers. Isentropic analyses of mixing ratio are generally far superior to horizontal or isobaric analyses. Also, isentropic analysis better captures the spatial integrity of elevated mixed layers and frontal structures, which also have distinct moisture signatures. The Barnes radius applied to radiosonde data was taken at the station spacing (~ 370 km) rather than twice the observed spacing because cross validation of selected soundings indicated that the analysis was able to reproduce the observed vertical structure only for a small Barnes radius for some cases and roughly equally in other cases. Observations with large discrepancies from the gridded data were rejected from the Barnes analysis. These analyses were then vertically interpolated onto a terrain-following σ - z grid with 150-m vertical grid spacing. Vertical mixing ratio gradients were computed from this grid and all of the data fed into Vis-5D [Hibbard, 1994] for visualizing the evolution of synoptic and mesoscale structures. The cross sections were generated by Vis-5D. The analyses extend well beyond the region shown in Figure 11.

Acknowledgments. We are grateful to Gregory Nasstrom of St. Cloud State University, who reviewed the manuscript for the editors, for his many constructive suggestions; to Robert Peters of Pennsylvania State University for making his software for analyzing ceilometer data available to us; and to Pete Pokrandt for assistance with data assimilation code used in conjunction with the University of Wisconsin Nonhydrostatic Modeling System. This work was supported by grants from the U.S. Office of Naval Research and the Canadian Atmospheric Environment Service.

References

- Barnes, S. L., Mesoscale objective analysis using weighted time-series observations, *NOAA Tech. Memo. ERL NSSL-62*, 66 pp., National Severe Storms Laboratory, Norman, Okla., 1973. (Available as COM-73-10781 from Natl. Tech. Inf. Serv., Springfield, Va.)
- Battan, L. J., *Radar Observation of the Atmosphere*, 324 pp., University of Chicago Press, Chicago, 1973.
- Chadwick, R. B., and K. P. Moran, Long-term measurements of C_n^2 in the boundary layer, *Radio Science*, **15**, 355–361, 1980.
- Courrier, P. E., Precipitation measurement using a dual frequency Doppler system, Ph.D. thesis, 242 pp., Univ. of Colo., 1990.
- Ecklund, W. L., D. A. Carter, and B. B. Balsley, A UHF wind profiler for the boundary layer: Brief description and initial results, *J. Atmos. Oceanic Technol.*, **5**, 432–441, 1988.
- Ecklund, W. L., D. A. Carter, B. B. Balsley, P. E. Currier, J. L. Green, B. L. Weber, and K. S. Gage, Field tests of a lower tropospheric wind profiler, *Radio Sci.*, **25**, 899–906, 1990.
- Flock, W. L., S. D. Slobin, and E. K. Smith, Propagation effects on radio range and noise in Earth-space telecommunications, *Radio Sci.*, **17**, 1411–1424, 1982.
- Gage, K. S., Radar observations of the free atmosphere: Structure and dynamics, in *Radar in Meteorology*, edited by D. Atlas, pp. 534–574, American Meteorological Society, Boston, 1990.
- Gossard, E. E., A fresh look at the radar reflectivity of clouds, *Radio Sci.*, **14**, 1089–1097, 1979.
- Gossard, E. E., Measuring drop-size distributions in clouds with a clear-air-sensing Doppler radar, *J. Atmos. Oceanic Technol.*, **5**, 640–649, 1988.
- Gossard, E. E., Radar research on the atmospheric Boundary layer, in *Radar in Meteorology*, edited by D. Atlas, pp. 477–527, American Meteorological Society, Boston, 1990.
- Gossard, E. E., and R. G. Strauch, *Radar Observation of Clear Air and Clouds*, 280 pp., Elsevier, New York, 1983.
- Hibbard, W. L., B. E. Paul, D. A. Santek, C. R. Dyer, A. L. Battaiola, and M.-F. Voidrot-Martinez, Interactive visualization of earth and space science computations, *Computer*, **July**, 65–72, 1994.
- Hildebrand, P. H., and R. S. Sekhon, Objective determination of the noise level in Doppler spectra, *J. Appl. Meteorol.*, **13**, 808–811, 1974.
- Hocking, W. K., Measurement of turbulent energy dissipation rates in the middle atmosphere by radar techniques: A review, *Radio Sci.*, **20**, 1403–1422, 1985.
- Knight, C. A., and L. J. Miller, First radar echoes from cumulus clouds, *Bull. Am. Meteorol. Soc.*, **74**, 179–188, 1993.
- Ottersten, E., Mean vertical gradient of potential refractive index in turbulent mixing and radar detection of CAT, *Radio Sci.*, **4**, 1247–1249, 1969.
- Pauley, P. M., and X. Wu, The theoretical, discrete, and actual response of the Barnes objective analysis scheme for one- and two-dimensional fields, *Mon. Weather Rev.*, **118**, 1145–1163, 1990.
- Rogers, R. R., W. L. Ecklund, D. A. Carter, K. S. Gage, and S. A. Ethier, Research applications of a boundary-layer wind profiler, *Bull. Am. Meteorol. Soc.*, **74**, 567–580, 1993.
- Rogers, R. R., S. A. Cohn, W. L. Ecklund, J. S. Wilson, and D. A. Carter, Experience from one year of operating a boundary-layer profiler in the center of a large city, *Ann. Geophys.*, **12**, 529–540, 1994.
- Smith, P. L., Scattering of microwaves by cloud droplets, paper presented at 11th Weather Radar Conference, Am. Meteorol. Soc., Boston, Sept. 14–18, 1964.
- Tatarski, V. I., *Wave Propagation in a Turbulent Medium*, 285 pp., McGraw-Hill, New York, 1961.
- Wakasugi, K., A. Mizutani, M. Matsuo, S. Fukao, and S. Kato, A direct method of deriving drop-size distribution and vertical air velocities from VHF Doppler radar spectra, *J. Atmos. Oceanic Technol.*, **3**, 623–629, 1986.
- D. A. Carter, W. L. Ecklund, and J. S. Wilson, Aeronomy Laboratory, NOAA, Boulder, CO 80303.
- S. A. Cohn and R. R. Rogers, Department of Atmospheric and Oceanic Sciences, McGill University, 805 Sherbrooke St. W., Montreal, Canada H3A 2K6. (e-mail: my29@musica.mcgill.ca)
- S. Jascourt, Department of Atmospheric and Oceanic Sciences, University of Wisconsin, Madison, WI 53706.

(Received March 17, 1994; revised November 7, 1994; accepted November 14, 1994.)